In-Situ Synchrotron X-ray Characterization of Corrosion Products in Zr Artificial Pits in Simulated Physiological Solutions

Yue Zhang,[a] Owen Addison,[b] Petre Flaviu Gostin,[a] Alexander Morrell,[c,d] Angus J. M. C. Cook,[a,e] Alethea Liens,[f] Jing Wu,[a] Konstantin Ignatyev,[d] Mihai Stoica,[g] and Alison Davenport[a,*,z]

[a]*School of Metallurgy and Materials, University of Birmingham, Edgbaston, Birmingham B15 2TT, United Kingdom*
[b]*Biomaterials Unit, School of Dentistry, University of Birmingham, Edgbaston, Birmingham B15 2TT, United Kingdom*
[c]*Aston Institute of Materials Research, Aston University, Birmingham B4 7ET, United Kingdom*
[d]*Diamond Light Source, Diamond House, Harwell Science and Innovation Campus, Didcot, Oxfordshire OX11 0DE, United Kingdom*
[e]*Wood, Harwell Campus, Oxfordshire OX11 0QB, United Kingdom*
[f]*Université de Lyon, INSA-Lyon, Laboratoire MATEIS, UMR CNRS 5510, 69621 Villeurbanne Cedex, France*
[g]*Laboratory of Metal Physics and Technology, Department of Materials, ETH Zurich, 8093 Zurich, Switzerland*

Corrosion products generated in artificial pits of zirconium were characterized in–situ by synchrotron X-ray diffraction and X-ray absorption near edge structure (XANES) in physiological saline, with and without addition of 4% albumin and/or 0.1% H_2O_2. Zr metal fragments and tetragonal ZrO_2 particles were detected in aggregated black corrosion products away from the corrosion front. At the corrosion front, a $ZrOCl_2{\cdot}8H_2O$ salt layer of a few hundreds of microns thickness was formed. Coarsened $ZrOCl_2{\cdot}8H_2O$ crystallites were found farther out into the solution. The Zr solution species were confirmed to be in a tetravalent state by XANES. TEM imaging of the corrosion products revealed heterogeneity of the morphology of the Zr metal fragments and confirmed their size to be less than a few microns. The formation and speciation of Zr corrosion products were found not affected by the presence of H_2O_2 and/or albumin in physiological saline. Furthermore, bulk Zr electrochemistry identified that the presence of H_2O_2 and/or albumin did not affect passive current densities and pitting potentials of the bulk Zr surface. Therefore, it is concluded that the pitting susceptibility and pit chemistry of Zr in physiological saline were unaffected by the presence of H_2O_2, albumin or their combinations.
 [DOI: 10.1149/2.0671714jes]

Manuscript submitted September 14, 2017; revised manuscript received November 17, 2017. Published December 1, 2017.

Zr is an element that is a common constituent of alloys used to manufacture biomedical implants.[1,2] Zr has been used in Ti-alloys to provide improved mechanical properties for surgical implants such as increased strength, e.g. Ti-5Zr,[3,4] or lower Young's modulus, e.g. Ti-3Zr-13Nb,[5,6] Ti-20Nb-10Zr-5Ta[7] and Ti-12Mo-6Zr-2Fe.[8] Furthermore, Zr-based biomedical alloys including Zr-Nb[9,10] and Zr–Mo[11] have been proposed for use where magnetic resonance imaging is anticipated, as Zr has low magnetic susceptibility. There is also considerable interest in Zr-based bulk metallic glasses. A number of Zr-based glass forming alloys have been described and offer the possibility of improved mechanical properties and chemical stability.[12–14]

Zr forms a spontaneous passive surface oxide film in air which protects it from further corrosion. However, Zr is susceptible to pitting attack, especially in halide ion containing environments.[15,16] Accordingly, a number of studies have shown the pitting susceptibility of Zr-based alloys including metallic glasses in chloride–containing simulated physiological solutions.[14,17] If implants in the body undergo pitting, free metal ions and other corrosion products may be released into the surrounding tissue where they can stimulate adverse biological reactions.[18,19] There is increasing concern over the long-term health effects of corrosion product accumulation in peri-implant tissue. As a consequence, there is a need to understand the corrosion mechanisms of biomedical alloys that occurs in-vivo, including tribo-corrosion and mechanically-assisted crevice corrosion (MACC) as well as corrosion independent of mechanical damage such as pitting.[20–24] Furthermore, it is important to identify possible corrosion products so that these can be simulated and used for in-vitro studies of cellular response.

Recent work by Yu et al. showed a significantly higher corrosion rate of Ti6Al4V in the presence of both H_2O_2 (produced in inflammatory reactions in peri-implant environment) and albumin (the most abundant protein in blood plasma), when compared with either species alone.[25] The increased corrosion of Ti6Al4V exacerbated by addition of albumin in the presence of H_2O_2 in physiological saline (i.e. 0.9% NaCl) solutions has been proposed to be attributed to enhanced dissolution caused by adsorption of albumin, which suppresses the cathodic reaction and shifts the open circuit potential to the active region of Ti6Al4V.[25] The increased corrosion rates induced by H_2O_2 and albumin highlights the complex roles that biomolecules have in mediating corrosion at the implant surface. More recently, very limited work has been carried out on the role of organic species including glycine[26] and albumin[27,28] on corrosion of Zr. Both species were demonstrated to adsorb onto the metal surface but contradictory effects (suppressing or accelerating) were claimed on the corrosion of Zr.[26,27] It has also been reported that the presence of H_2O_2 reduces the corrosion resistance of thermally oxidized Zr5Ti where surface oxides are mostly composed of ZrO_2.[29] No studies have been reported on the combined effect of H_2O_2 and albumin in terms of corrosion and corrosion products. Therefore, the role of H_2O_2 and/or albumin on corrosion of Zr and the resulting corrosion products are considered in this study.

In this work, the effects of H_2O_2, albumin and combination of the two species in 0.9% NaCl on the electrochemistry of Zr and formation of corrosion products were investigated. The structure and speciation of corrosion products formed on dissolving Zr surfaces in simulated physiological solutions were characterized in-situ by synchrotron X-ray diffraction (XRD) and X-ray absorption near edge structure (XANES), and the morphology and size of ex-situ corrosion products was determined with TEM. The dissolving Zr interface was formed by growing a Zr "artificial pit", a method that is commonly used to model localized corrosion processes.[30–32] The findings shed light on possible degradation products that might accumulate in the body environment around Zr-containing implants.

Experimental

Materials and sample preparation.—Electrochemical cells were prepared according to the method described by Rayment et al.[33] The working electrode was made from 3 mm strips of Zr foil (25 μm thick) (Advent Research Materials, UK, 99.8 wt% Zr, temper annealed), which was embedded in Araldite epoxy resin and attached to a PVC plastic reservoir by Kapton adhesive tape. The reservoir contained a Ag/AgCl reference electrode, a Pt wire counter electrode

*Electrochemical Society Member.
[z]E-mail: a.davenport@bham.ac.uk

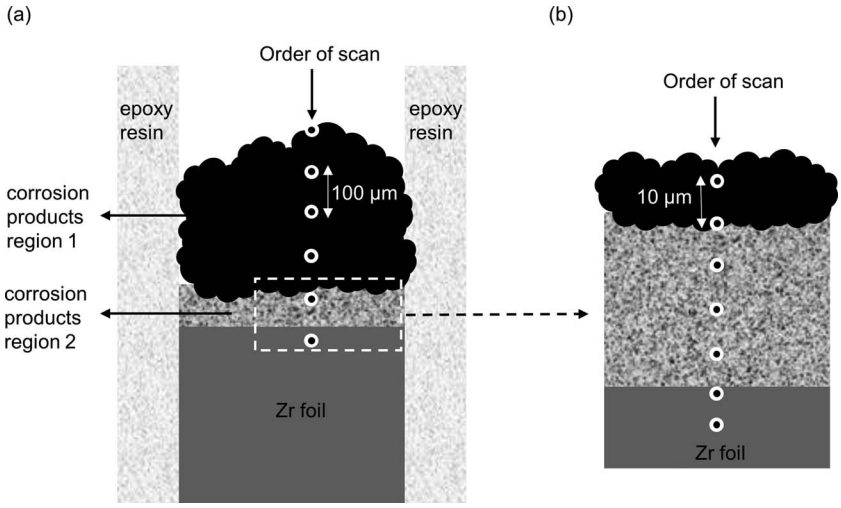

Figure 1. Schematic diagram of the XRD scan path through different regions of corrosion products inside Zr artificial pit. Numbers represent sequence of measurements. (a) order of a coarse XRD scan at 100 µm spacing from electrolyte through corrosion products into Zr foil; (b) order of a fine XRD scan at 10 µm spacing through corrosion products region 2 close to dissolving metal interface.

and electrolyte. The electrolytes were 20 mL of 0.9 wt% (or 0.15 M) NaCl with or without addition of 0.1 wt% (or 0.03 M) H_2O_2 (30 wt% in H_2O, Sigma Aldrich, UK) or 4 wt% albumin (≥98%, lyophilized powder, Sigma Aldrich, UK) or their combination. All potentials for artificial pits were referenced to anAg/AgCl electrode stored in a 3 M NaCl solution (−0.035 V vs. SCE). Prior to in-situ X-ray measurements, the working electrode was electrochemically dissolved at 0.8 V (Ag/AgCl) for ∼3 h at an ambient temperature of 23 ± 1°C. The potential was controlled by an Ivium Compactstat potentiostat.

X-ray diffraction.—In-situ X-ray diffraction measurements were conducted at the micro-focus spectroscopy beamline I18 at the Diamond Light Source (Harwell, Oxford, UK)[34] An incident X-ray photon energy of 17,950 eV (corresponding to a wavelength of 0.691 Å) and beam spot size of 3 µm (vertical) x 10 µm (horizontal) were used, and measurements were taken with a CCD detector (Photonic Science 2 × 1 sCMOS camera) providing a pixel size resolution of 26 µm x 26 µm. The electrochemical cell was mounted on a precise XYZ translation stage allowing sample interrogation to be undertaken at any location with respect to the corroding metal solution interface. Prior to measurements, the metal solution interface was placed in focus and the sample was positioned where the X-ray beam was in the electrolyte above any corrosion products. Diffraction patterns were collected from the electrolyte toward the metal solution interface by moving the sample stage up in 100 µm increments. A schematic diagram (Figure 1a) illustrates the approach which enabled the measurements of all different regions of the corroding interface to be made. Corrosion products close to the dissolving metal interface were also measured with a reduced step size of 10 µm (Figure 1b) enabling changes at a higher spatial resolution to be identified. Both sets of diffraction measurements were repeated in each electrolyte solution. The exposure time was limited to 30 s to reduce beam damage. The position of each diffraction pattern was correlated with a 'live' optical image of the corroding artificial pit to allow exact correlation of the diffraction pattern relative to the moving metal-electrolyte interface. X-ray diffraction patterns were integrated and analyzed in DAWN (Version 2.0.0, 2010–2016)[35] and FullProf software (Version 3.00, 2015).[36]

X-ray absorption near edge structure.—XANES measurements on solution Zr species and Zr standard compounds were made in fluorescence geometry on the same beamline (I18) immediately following XRD measurements. A Zr reference foil was used for energy calibration of all XANES measurements. Zr reference compounds i.e. ZrO_2 (98.5%, Fisher Scientific, UK), $ZrOCl_2{\cdot}8H_2O$ (reagent grade 98%, Scientific Laboratory Supplies, UK) and $Zr(OH)_4$ (97%, Sigma-Aldrich, UK) were prepared in as-received powder form. Additionally, $ZrOCl_2{\cdot}8H_2O$ powder was ground farther to reduce the crystallite size.

XANES spectra were obtained by scanning a Si (111) double crystal monochromator which produced a X-ray beam with energy ranging from 17,900 eV to 18,400 eV. The beam spot size was maintained at 3 µm (v) x 10 µm (h) focused by Kirkpatrick-Baez (KB) mirrors. Fluorescence data were collected using a 4-element Vortex Si drift detector. To generate a high signal to noise ratio, 206 energy points were used across the edge with an irradiation time of 1s per point. The resulting spectra were normalized using Athena software (Version 0.9.24).[37]

Ex-situ SEM and TEM.—The morphology of the dissolving surface from a Zr artificial pit was examined ex–situ by scanning electron microscopy (SEM) in secondary electron mode on a JEOL 7000 (Japan Electron Optics Laboratory Co., Ltd) using an operating energy of 20 keV. The corroded Zr artificial pit embedded in epoxy was immersed in methanol for 10 min to allow the epoxy resin to be removed. Exposed foil was cleaned with methanol and deionized water in ultrasonic bath each for 10 min, followed by mounting on an aluminum sample stub with the corrosion interface facing upwards. Corrosion products were characterized further by Transmission Electron Microscopy (FEI Talos) with an operating energy of 200 keV for high resolution chemical analysis and morphology characterization. Corrosion products were collected from a Zr artificial pit which was grown at 0.8 V (Ag/AgCl) in 0.9% NaCl for ∼3 h at ambient temperature. The collected corrosion products were rinsed with deionized water into a 30 mL plastic tube, where corrosion products settled after 24 h. The supernatant was discarded and the pellet of corrosion products was dispersed onto a gold TEM sample grid using a microliter syringe. The TEM sample grid with deposited corrosion products was placed in a desiccator before characterization.

Electrochemistry of bulk Zr samples.—CP Zr rods (Grade 702, GoodFellow, UK) (diameter 10 mm) were commercially sourced and machined into 1 mm thickness discs. Bulk Zr samples for electrochemical measurements were prepared and polished to a final surface finish of 0.04 µm using OP–S colloidal silica suspension (Struers, UK), complied with a previously described procedure.[25] Freshly prepared samples were immersed in 0.9% NaCl with or without addition of 0.1% H_2O_2 or 4% albumin or their combination at 37 ± 1°C. Following immersion, Open circuit potentials (OCP) were measured for 1 h followed by potentiodynamic polarization from −50 mV (vs. OCP) at a rate of 1 mV/s. The current limit was set at 0.1 mA/cm^2 at which the measurement was stopped. Two measurements were repeated for each solution. Samples after polarization tests were stored in a desiccator prior to SEM characterization.

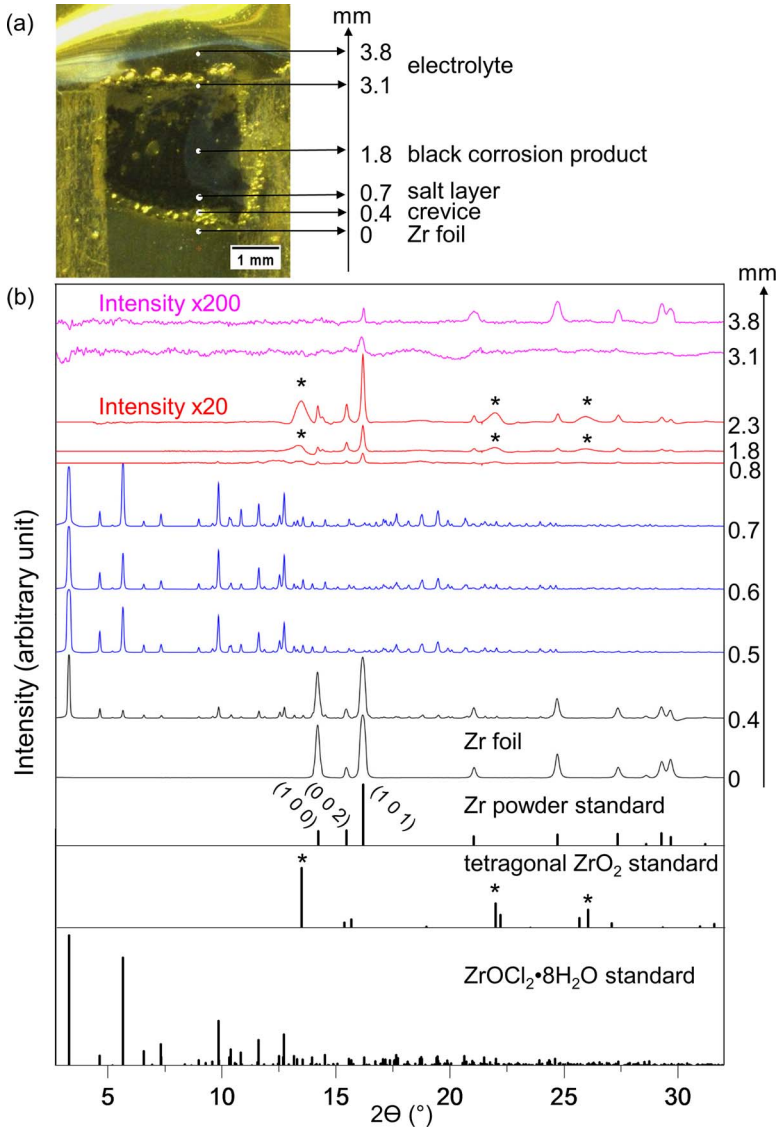

Figure 2. (a) Optical image of a Zr artificial pit at 0.8 V (Ag/AgCl) in 0.9% NaCl + 4% albumin + 0.1% H_2O_2 solution at ambient temperature. The height of XRD measurements above the dissolving interface are marked; (b) stack plot of selected diffraction patterns in a sequence from solution to metal. Intensities of diffraction patterns at 3.8 and 3.1 mm were multiplied by 200x and intensities of diffraction patterns at 2.3, 1.8, 0.8 mm in black corrosion products were multiplied by 20x. Standards for Zr powder,[38] tetragonal ZrO_2[39] and $ZrOCl_2{\cdot}8H_2O$[40] are indicated. ∗Peaks that correlate with ZrO_2.

Results

Overall structure of corrosion products.—Figure 2a shows an optical image of a ∼3 mm deep Zr artificial pit that was grown at 0.8 V (Ag/AgCl) in physiological saline (0.9% NaCl) solution with addition of 0.1% H_2O_2 and 4% albumin. The location of XRD measurements relative to the position of the Zr foil (0 mm) are noted. Diffraction patterns are shown as a stack plot in Figure 2b, and their positions are referenced to the locations marked in Figure 2a. The diffraction pattern of Zr foil at 0 mm (Figure 2b) was consistent with a Zr powder standard[38] but with different relative heights of peaks due to the anisotropy of the foil. At 0.4 mm, where it was apparent a crevice had formed between the foil and the embedding epoxy (Figure 2a), the diffraction pattern shows the presence of Zr metal (foil) and zirconyl chloride octahydrate ($ZrOCl_2{\cdot}8H_2O$).[40] From 0.5 to 0.7 mm, more intense diffraction peaks consistent with the $ZrOCl_2{\cdot}8H_2O$ standard were observed. From 0.8 to 2.3 mm, which corresponds to black corrosion products in the optical image (Figure 2a), the diffraction was weaker, but the major diffraction peaks (intensity 20x) are consistent with a Zr powder standard[38] and three broad peaks indicated with asterisks are consistent with three major peaks of the tetragonal ZrO_2 standard.[39] At 3.1 and 3.8 mm, corresponding to electrolyte inside and outside of the pit cavity (Figure 2a), the diffraction peaks (intensity 200x) are shown to be consistent with that of the Zr powder standard.[38]

Structure of black corrosion products farther away from the corrosion front.—Figure 3a shows an optical image of a Zr artificial pit at 0.8 V (Ag/AgCl) in 0.9% NaCl. It can be seen that black corrosion products accumulated at the left-hand side 'bulge' of the pit cavity. The 'bulge' feature enabled measurements to be made of corrosion products that were not located at the position of the original Zr foil. Figure 3b shows a stack plot of the selected normalized diffraction patterns at 2.2 mm, 1.8 mm, and an average of all patterns from 0 to 3 mm. It was found that the location of all major peaks from the selected patterns were consistent with the Zr powder standard.[38] Furthermore, the relative heights of the peaks from the corrosion products were more consistent with the Zr powder standard than the anisotropic foil, suggesting that the corrosion products are randomly-oriented Zr metal fragments. In addition to sharp Zr metal peaks, fainter broad peaks were consistently observed (marked with asterisks), and from the averaged diffraction pattern (Figure 3c), it was found that the peaks were consistent with the tetragonal ZrO_2 standard.[39]

Figure 4a shows the diffraction pattern of the Zr foil with clear anisotropy in the (0 0 2), (1 0 0) and (1 0 1) reflections highlighted. Figures (b), (c) and (d) show diffraction patterns of the Zr fragments found in the black corrosion products. Figures 4b and 4c show less anisotropy and a different preferential orientation of crystals, suggesting that fragments may have rotated after they became detached. The average of the diffraction patterns from 0 mm to 3 mm (Figure 4d) shows isotropic scattering with continuous and smooth diffraction

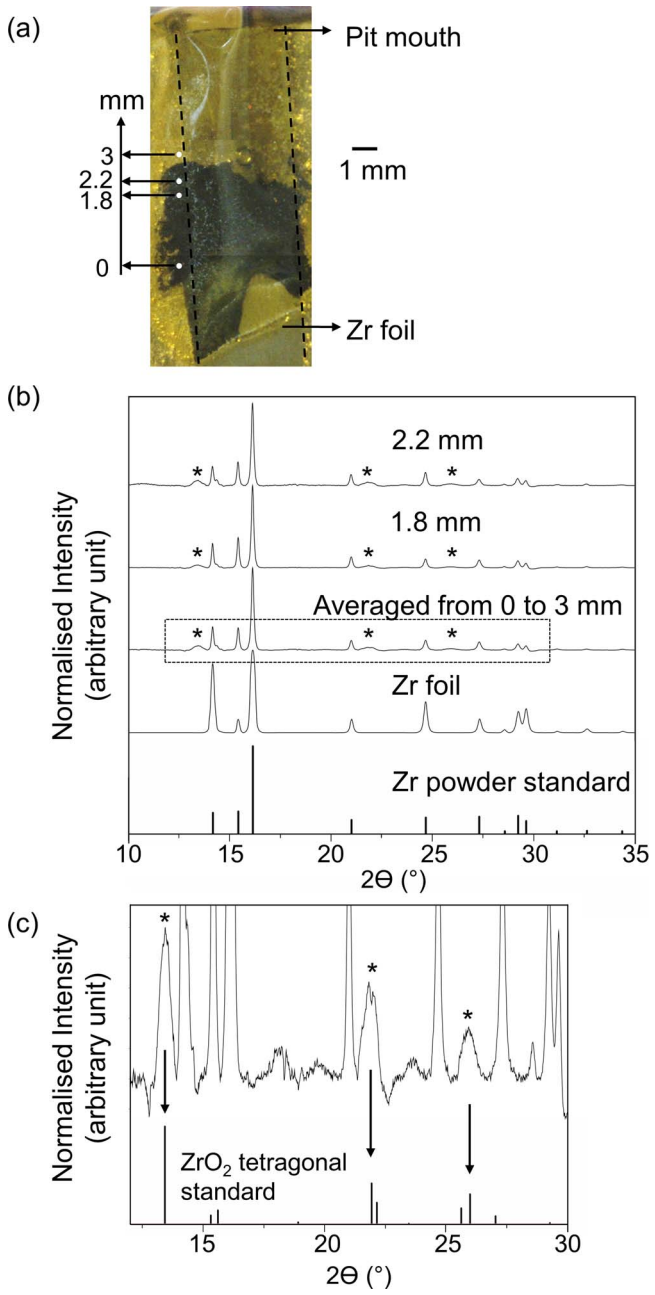

Figure 3. (a) Optical image of a Zr artificial pit at 0.8 V (Ag/AgCl) in 0.9% NaCl at ambient temperature. The location of selected diffraction patterns from a XRD scan with 100 μm step-size are shown at the left-hand side 'bulge' of the artificial pit are shown (mm) relative to 0 mm indicated at the bottom; (b) diffraction patterns at 2.2 mm and 1.8 mm (locations marked in (a)), the average of all patterns from 0 mm to 3 mm, and the Zr foil. Intensities were normalized to the maximum Zr peak. Peaks marked with asterisks are shown in detail in (c) with intensity normalized to the maximum ZrO_2 peak. The Zr powder standard[38] and tetragonal ZrO_2 standard[39] are indicated at the bottom of (b), and (c), respectively.

rings at all planes, suggesting many fine randomly oriented crystallites.

Structure of salt layer close to the corrosion front.—Figure 5a shows an optical image of a Zr artificial pit with magnified views of the salt layer for the sample containing 0.9% NaCl + 0.1% H_2O_2. The dissolving interface is not flat: there appears to have been some crevice corrosion. The point marked 0 μm is the highest point that appears to have no crevice corrosion, gives only rings from the foil (also see in the diffraction pattern shown in supporting material Figure S1). At 100 μm, there are strong diffraction rings from the foil (indicated with upward arrows) showing characteristic anisotropy (Figure 5b), but also a few rings that are characteristic of $ZrOCl_2{\cdot}8H_2O$ (supporting material Figure S1) (indicated with diagonal arrows). The presence of rings from both the Zr foil and $ZrOCl_2{\cdot}8H_2O$ indicates that there is crevice corrosion down the interface between the epoxy and the foil. At 130 μm (Figure 5c), more intense and smooth diffraction rings of $ZrOCl_2{\cdot}8H_2O$ were observed. At 570 μm (Figure 5d), farther away from the interface, $ZrOCl_2{\cdot}8H_2O$ was also observed, but diffraction rings were found to be spotty, indicating coarsening of the salt crystals. At 680 μm (Figure 5e), even farther away from the interface and close to the black corrosion products, the diffraction pattern exhibited discrete speckles consistent with coarse crystals of $ZrOCl_2{\cdot}8H_2O$ and faint diffraction rings from Zr metal indicating the presence of Zr fragments, which was consistent for all solutions studied. $ZrOCl_2{\cdot}8H_2O$ was consistently observed from the dissolving surface to a distance of approximately 500 μm to 600 μm away from the interface with gradual coarsening of the salt crystals farther into the solution.

XANES spectrum of solution species in the pit cavity.—Figure 6a shows a series of normalized XANES spectra for solution species in a Zr artificial pit grown in at 0.8 V (Ag/AgCl) in 0.9% NaCl + 4% albumin + 0.1% H_2O_2 as well as Zr reference compounds. The spectra of the Zr^{4+} reference compounds are spectroscopically very similar, and show identical features to the spectra of the artificial pit solution species: a relatively featureless edge with an absorption edge peak at 18,020 eV and a weak pre-edge peak, more easily observed in first derivative (Figure 6b), at 18,000 eV. This confirms that the solution species in the artificial pit is Zr in the tetravalent state, but no further information on its co-ordination environment can be inferred.

Ex-situ Microscopy of Zr Corrosion Products and its Dissolving Interface

SEM image of dissolving Zr interface.—Figure 7 shows SEM images of different regions of the Zr surface from an artificial pit grown at 0.8 V (Ag/AgCl) in 0.9% NaCl + 4% albumin + 0.1% H_2O_2 for approximately 5 h. It can be seen that the corroding interface shows a high level of roughness (Figure 7a), and in some areas localized variations of roughness were also observed (Figure 7b).

TEM of Zr corrosion products.—TEM with EDX was used to identify the chemical composition and morphologies of corrosion products collected from a Zr artificial pit cavity (Figure 8). EDX confirmed the presence of Zr metal particles with a composition of 98.9 ± 0.2 wt% Zr (∗, Figure 8). Some metal fragments appeared to show some directionality to the dissolution, with parallel strips of metal with sizes up to 2 μm, although smaller fragments (mostly several hundred nanometers) were seen. The compositions of corrosion products (⊙, Figure 8) showed 82 wt% of Zr and 18 wt% of O (44 at% of Zr and 56 at% of O), suggesting the presence of Zr oxides/hydroxides. It can be seen that these Zr oxides/hydroxides are in a "mesh" morphology engulfing the metal particles.

Electrochemical polarization on bulk Zr surfaces.—Figure 9a shows anodic polarization curves for bulk Zr samples in 0.9% NaCl solution with or without addition of H_2O_2 and/or albumin. It can be seen that the open circuit potential of Zr in 0.9% NaCl was shifted to more positive values by addition of H_2O_2, and slightly shifted in the negative direction by the addition of albumin. The open circuit potentials in the presence of both H_2O_2 and albumin were found to be between those in solutions containing H_2O_2 or albumin individually. The bulk Zr samples were passive with current densities in the range of 3 to 10 μA/ cm^2 for all solutions up to approximately 500 mV (vs. SCE), at which point the current density increased rapidly above the "pitting potential". Figure 9b shows pitting potentials in the different testing solutions, which varied from 550 to 1000 mV (vs. SCE) and

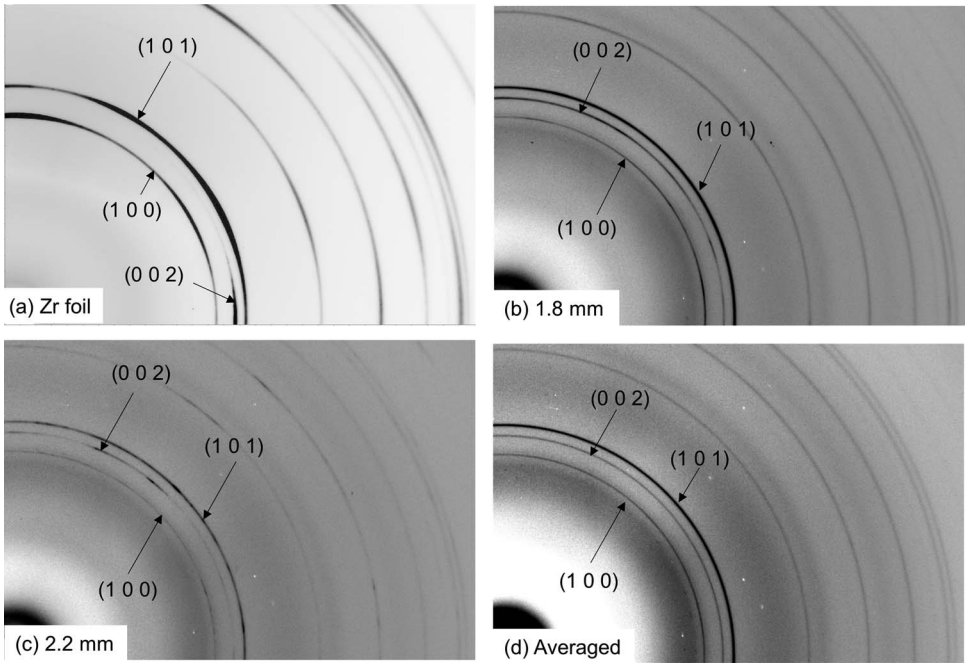

Figure 4. Diffraction pattern images at positions as shown in Figure 3. Image (b), (c) and (d) are shown with adjusted brightness and contrast.

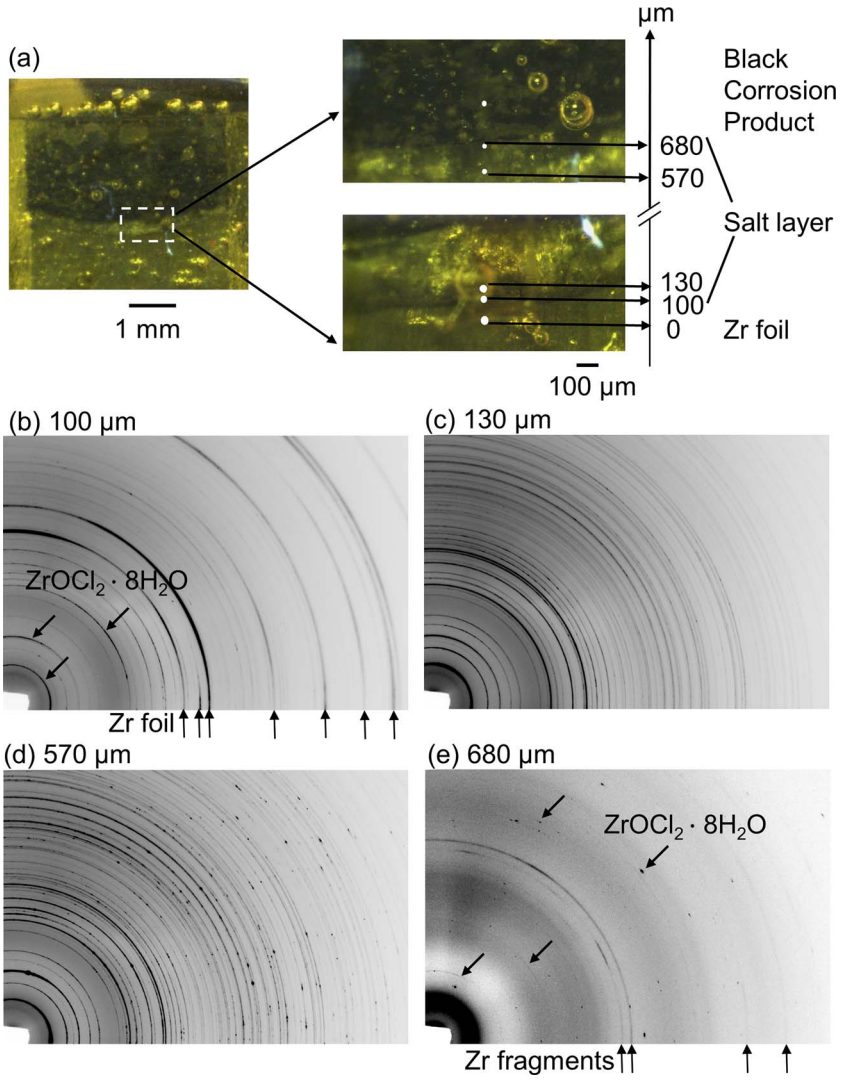

Figure 5. (a) Optical image of a Zr artificial pit at 0.8 V (Ag/AgCl) in 0.9% NaCl + 0.1% H_2O_2 at ambient temperature. (b)-(e) Diffraction patterns from a 10 μm step line scan in a sequence from the black corrosion products through the salt layer and into the metal. Positions of the selected patterns are referenced in μm with respect to the top of the uncorroded Zr foil (0 mm). Arrows shown diagonally indicate diffraction rings from $ZrOCl_2{\cdot}8H_2O$ phase; arrows shown upwards indicate diffraction from Zr metal. Diffraction images at (b) 100 μm; (c) 130 μm; (d) 570 μm and (e) 680 μm are shown with adjusted brightness and contrast.

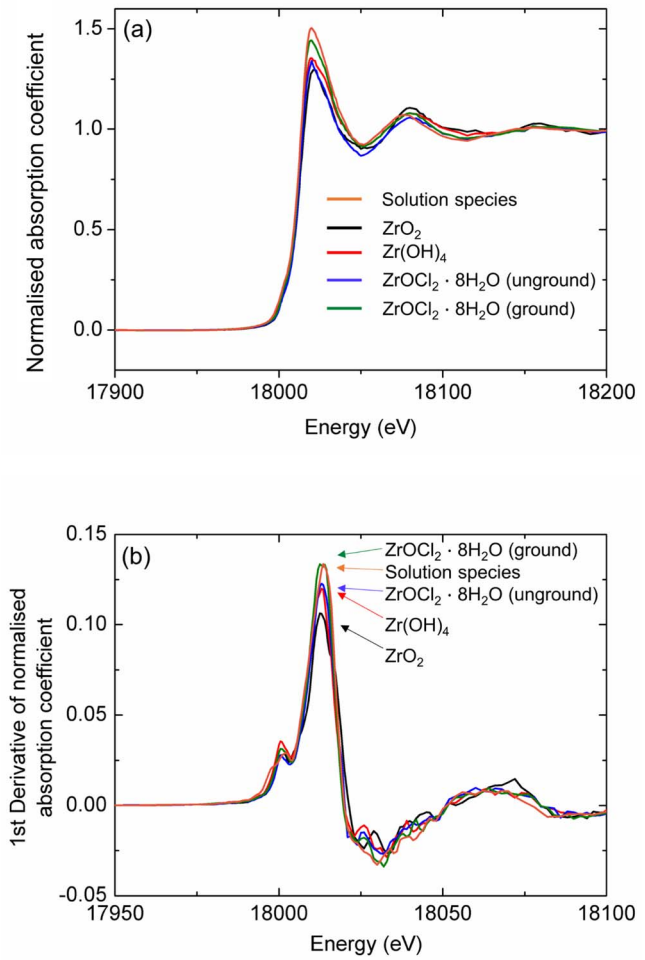

Figure 6. (a) Normalized XANES spectrum of solution species as well as Zr reference compounds ZrO_2, $Zr(OH)_4$, as received and ground $ZrOCl_2{\cdot}8H_2O$, the solution spectra were measured from in the pit cavity of the Zr artificial pit shown in Figure 2; (b) first derivative of the spectra shown in (a).

were found to be similar regardless of the presence of H_2O_2 and/or albumin in 0.9% NaCl.

Figure 10 shows pit morphologies on bulk Zr samples after anodic polarizations in 0.9% NaCl with and without presence of H_2O_2 and/or albumin. It was observed that pit surfaces exhibited varying localized roughness in all solutions, regardless of the presence of H_2O_2 and/or albumin in 0.9% NaCl. At higher magnifications, localized areas inside the pit showed honeycomb-like structure, consistent with undercutting processes likely to lead to the formation of metal fragments (e.g. Figure 10b as indicated by arrows).

Discussion

Zr metal fragments.—Zr metal fragments were detected in-situ by XRD in the pit cavity (Figure 2b), including at locations in the pit 'bulges' at some distance from the original location of the bulk foil (Figure 3b). The original foil showed distinctive anisotropy (Figure 4a) owing to the preferential alignment of crystals with the rolling direction during manufacture. The Zr fragments in individual point measurements showed some anisotropy but with different orientations (Figure 4b and c), whereas the average of a number of diffraction patterns through the thickness of the corrosion product layer (Figure 4d), was more consistent with a Zr powder standard.[38] TEM was subsequently used to characterize the corrosion products (Figure 8) and Zr metal fragments were identified by EDX analysis. Some metal fragments were found to show parallel strips (Figure 8), which might be associated with crystallographic dissolution.

The dissolving interface of Zr exhibited a high level of roughness for both Zr artificial pits, and pits on bulk Zr samples after anodic polarization (Figure 7a and Figure 10). A similar observation was reported by Palit and Gadyar[15] who showed that the dissolving surfaces of Zr pits were irregular exhibiting a 'spongy' morphology. It was also claimed that in the active growing pit, 'a black powder' was formed which was shown to contain α–zirconium by X-ray analysis,[41] supporting the findings of this study. Although the dissolving interface was highly roughened at multiple locations, there was also variation in roughness across localized areas (Figure 7b).

Based on the XRD measurements, the sub–micron size and fragmented morphologies of Zr fragments, and the highly roughened dissolution surfaces, it can be speculated that Zr metal fragments are produced by an undercutting mechanism which is well established in stainless steel systems.[42] Pits on stainless steel grow by undercutting of the passive metal surface. The upward growth of lateral lobes perforates the metal surface and produces metal particles leaving a porous cover known as a 'lacy cover'.[42] Similar observations on the formation of metal particles as a result of dissolution process have been reported in commercially pure (CP) Ti artificial pits.[43] Micron–sized Ti metal particles were detected from a pit cavity, generated by only an electrochemical corrosion process. It was proposed that pits only propagate at the front where the metal ion concentration is sufficiently high, while the remaining pit surface is passive, and the propagating front grows by undermining the metal and perforating surface generating metal particles.[43]

$ZrOCl_2{\cdot}8H_2O$.—$ZrOCl_2{\cdot}8H_2O$ was identified at the corrosion front, in the artificial pit and formed a salt layer a few hundred microns thick above the dissolving interface (Figure 2b and Figure 5). Crystal coarsening was observed farther out into the solution. Hydrated Zr^{4+} ions are reported to be stable in strongly acidic solutions (1 M) and in a concentration lower than 10^{-4} M.[44,45] In more concentrated and/or less acidic solutions, Zr^{4+} will undergo a vigorous hydrolysis reaction and forms zirconyl ions i.e. $[Zr_4(OH)_8{\cdot}16H_2O]^{8+}$ that are kinetically stable.[46] In chloride containing environments, the zirconyl ions can form zirconyl chloride octahydrate ($ZrOCl_2{\cdot}8H_2O$) which was observed as the dominant species in the XRD data.

The zirconyl species $[Zr_4(OH)_8{\cdot}16H_2O]^{8+}$ is a complex, consisting of four Zr atoms in the corners of slightly distorted square plane and linked by double hydroxo bridges. Four additional water molecules are bound to each Zr atom so that the Zr atom is coordinated by eight O atoms in a distorted square antiprism.[40] The remaining water molecules and chloride ions form a matrix which holds the zirconyl complexes together to form $ZrOCl_2{\cdot}8H_2O$.[40]

Tetragonal ZrO_2.—Tetragonal ZrO_2 was detected in-situ in regions where black corrosion products were visible (Figure 2 and Figure 3). Broadening of the diffraction peaks of tetragonal ZrO_2 (marked with asterisks in Figure 2b and Figure 3b) is likely to be attributable to particle size broadening. The ZrO_2 crystallite size was estimated using the Sherrer equation to be ~10 nm based on the averaged diffraction pattern shown in Figure 3b.[47] The size estimation was consistent with TEM observations which were consistent with the presence of nano–scale zirconium oxides/hydroxides (82% Zr and 18% O in wt%, Figure 8).

Nano-scale ZrO_2 particles can be synthesized by hydrolysis of an aqueous solution of $ZrOCl_2{\cdot}8H_2O$.[48,49] Hydrolytic polymerization of $ZrOCl_2{\cdot}8H_2O$ solutions produces a hydrated amorphous gel of ZrO_2, which can be transformed into crystalline phases such as monoclinic and tetragonal ZrO_2 on heating, with the phase formed dependent on the precipitation conditions.[49] It is reported that the crystal structure of ZrO_2 is dependent on the pH of the precipitation solution and the time taken to attain this pH, although the thermodynamic stable phase of crystalline ZrO_2 is monoclinic at room temperature.[49,50] Tetragonal ZrO_2 was found to be formed more effectively in precipitation solutions of higher pH and with slower precipitation rates.

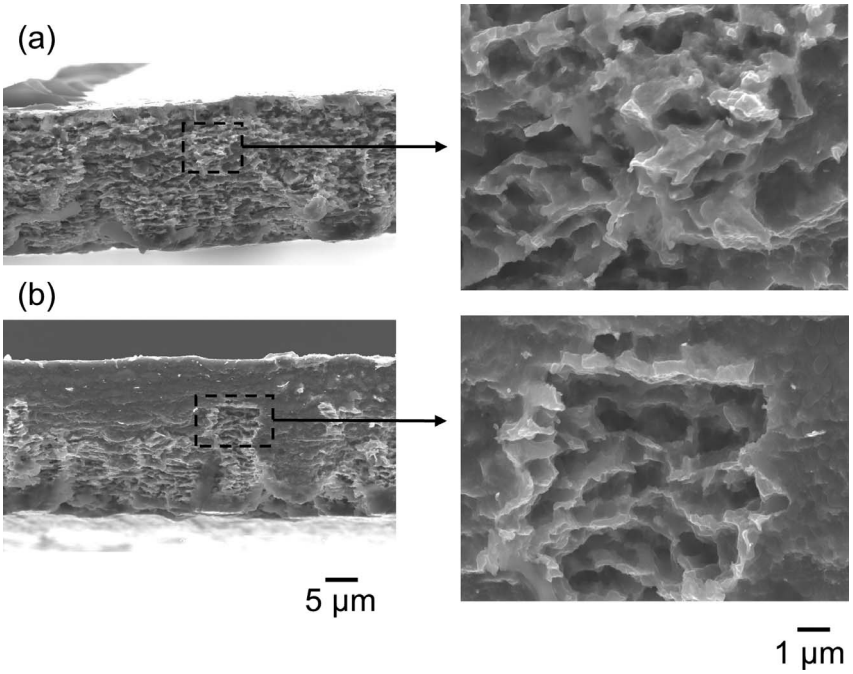

Figure 7. SEM images of different regions (a and b) of the top surface of a Zr artificial pit grown at 0.8 V (Ag/AgCl) in 0.9% NaCl + 4% albumin + 0.1% H_2O_2 for approximately 5 h at ambient temperature.

Further studies also propose that the tetragonal phase can be stabilized against transformation to monoclinic if the particle size is less than 30 nm.[49–51] In this study, tetragonal ZrO_2 was found dispersed above the $ZrOCl_2{\cdot}8H_2O$ salt layer toward the pit mouth (less acidic compared with the solution deep in the pit) when Zr artificial pits were grown for 3–5 h. Although the exact formation mechanism is not fully understood as there is no thermal factor evident, it is not unreasonable to propose that less acidic pH conditions found toward the pit mouth and a slow precipitation process facilitated the formation of tetragonal ZrO_2 by polymeric hydrolysis of $ZrOCl_2{\cdot}8H_2O$ solutions.[49,50]

The effect of H_2O_2 and/or albumin on formation of Zr corrosion products and biomedical implications.—As seen in Figure 9, the addition of H_2O_2 and/or albumin in physiological saline did not have a significant effect on the passive current densities and pitting potentials of the bulk Zr samples. A comparison of pit morphologies showed a similar characteristic 'honeycomb' morphology as well as rough pit surface regardless of the presence of H_2O_2 and/or albumin in physiological saline (Figure 10). In-situ XRD characterization of Zr corrosion products at 0.8 V (Ag/AgCl) demonstrated the generation of the same corrosion species i.e. Zr metal fragments, tetragonal ZrO_2 and $ZrOCl_2{\cdot}8H_2O$ in the saline with or without addition of H_2O_2 and/or albumin (supporting material Figure S2). Similarly, identical corrosion species were also observed in Zr artificial pits growing at 1.3 V (Ag/AgCl), suggesting replication of the pit chemistry at higher potentials. Therefore, it can be concluded that H_2O_2 and/or albumin induces very limited effects on pitting susceptibility and pit chemistry of Zr in physiological saline. The behavior of Zr is different from that of Ti alloys, where the combined effect of H_2O_2 and albumin have a significant effect on corrosion of Ti6Al4V.[25] Ti and TiO_2 are known to form complexes with H_2O_2 and as a result, rougher and thicker oxides are formed, which enhance subsequent albumin adsorption.[52] In contrast, Zr is more resistant to degradation in the presence of H_2O_2,[29] owing to the stable and compact ZrO_2 oxide film. The accelerated dissolution of Ti6Al4V by H_2O_2 and albumin has been attributed to the albumin-catalysed dissolution of corrosion product layer resulting in formation of a thinner oxide film.[53] In contrast, the stable ZrO_2 surface oxide film is less likely to form complexes with albumin.

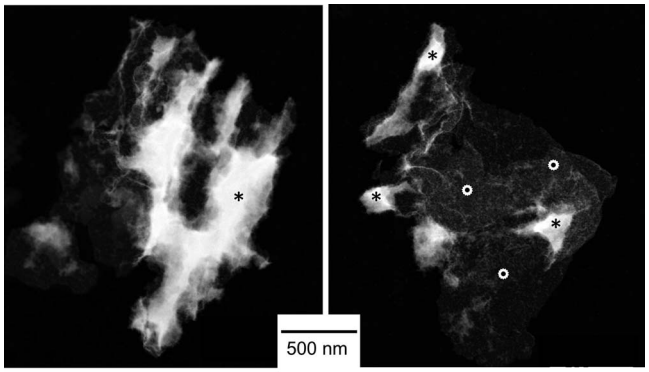

wt%	Zr	O	n
*	98.9 ± 0.2	1.1 ± 0.2	3
⊙	82 ± 2	18 ± 2	4

Figure 8. TEM images (dark field) of corrosion products from Zr artificial pit after growing at 0.8 V (Ag/AgCl) in 0.9% NaCl for 3 h at ambient temperature. Positions of EDX point analysis are marked with * and ⊙, and relative compositions (wt%) are shown in the Table with mean values and standard deviation (based on the number of measurements, n).

Corrosion products, including small micron and sub-micron sized metal particles, have frequently been identified in retrieved peri-implant tissues associated with a variety of devices and metal substrates, including devices that are not expected to be at risk of mechanical damage.[21,23,24] It is also accepted that the implant degradation products induce inflammatory responses in the peri–implant environment, leading to adverse clinical outcomes such as bone resorption and aseptic loosening.[22] Understanding the in-vivo corrosion mechanism of metallic implants is vital, however, and still remains an open questions. In the present work, we demonstrated metal fragments can be generated as a result of a purely electrochemical corrosion process, indicating the generation of metal fragments in the absence of wear. Future work needs to be carried out to improve the understanding of in-vivo corrosion mechanism of implant devices, especially the role of electrochemical degradation, in order to make reliable predictions of their performance in the body.

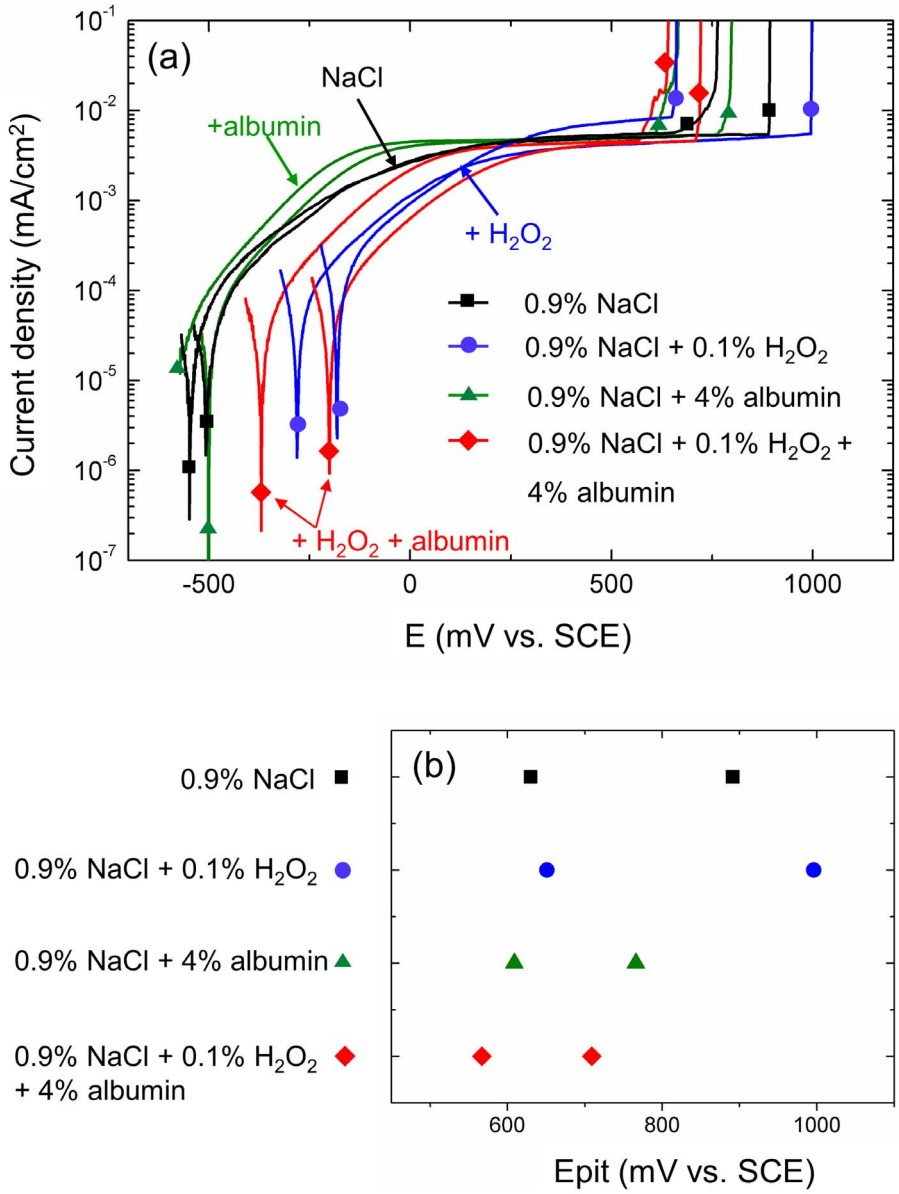

Figure 9. (a) Anodic polarization of bulk Zr samples in 0.9% NaCl with and without addition of 0.1% H_2O_2 and/or 4% albumin at 37 ± 1°C after 1 h at open circuit potential. Scan rate was 1 mV/s. Potentials are referenced to standard calomel electrode (SCE). (b) Pitting potentials from the data shown in (a), as the potential at 0.1 mA/cm^2 was reached. Two repetitions were given for each solution.

Conclusions

In-situ synchrotron X-ray diffraction and XANES were used to characterize corrosion products in Zr artificial pits in 0.9% NaCl (physiological saline) with the presence or absence of 0.1% H_2O_2, or 4% albumin, or their combinations.

In a solution of 0.9% NaCl with both 0.1% H_2O_2 and 4% albumin, Zr fragments and tetragonal ZrO_2 were found dispersed further away from the corroding interface, and $ZrOCl_2{\cdot}8H_2O$ crystallites were found close to the corroding interface and coarsened further out into the solution. XANES measurements in the solution gave a spectrum that was identical to a number of Zr reference compounds, which confirms Zr solution species are in tetravalent state.

Diffraction patterns for Zr foil were anisotropic whereas Zr fragments gave an isotropic pattern, which suggests that as-produced fragments were randomly oriented and dispersed in the pit cavity. TEM on corrosion products showed the morphology of Zr fragments in a submicron size. SEM on the dissolved surface of a Zr artificial pit showed a highly-roughened dissolution interface with variability in roughness in the localized areas. Therefore, it is likely that Zr fragments are produced via an undercutting mechanism.

The corrosion products were not affected by the presence or absence of H_2O_2, or albumin, or their combinations in 0.9% NaCl.

Anodic polarization of bulk Zr samples in physiological saline exhibited similar passive current density and pitting potentials in both the absence and presence of H_2O_2, albumin and their combinations. SEM images showed similar pit morphology compared across the different solutions. Therefore, H_2O_2 and albumin are proposed to have limited effects on bulk electrochemistry of Zr and its pitting susceptibility.

Acknowledgments

This work was supported by Prof. Addison's funding from the National Institute for Health Research, award No. NIHR/CS/010/001. Yue Zhang received a postgraduate research scholarship from the University of Birmingham School of Metallurgy and Materials. We thank Diamond Light Source for access to Beamline I18 (proposal SP13963) that contributed to the results presented here. Dr Steven Street is acknowledged for help on artificial pit experiments. This project has received funding from the European Union's Horizon 2020 research and innovation programme under the Marie Sklodowska-Curie grant

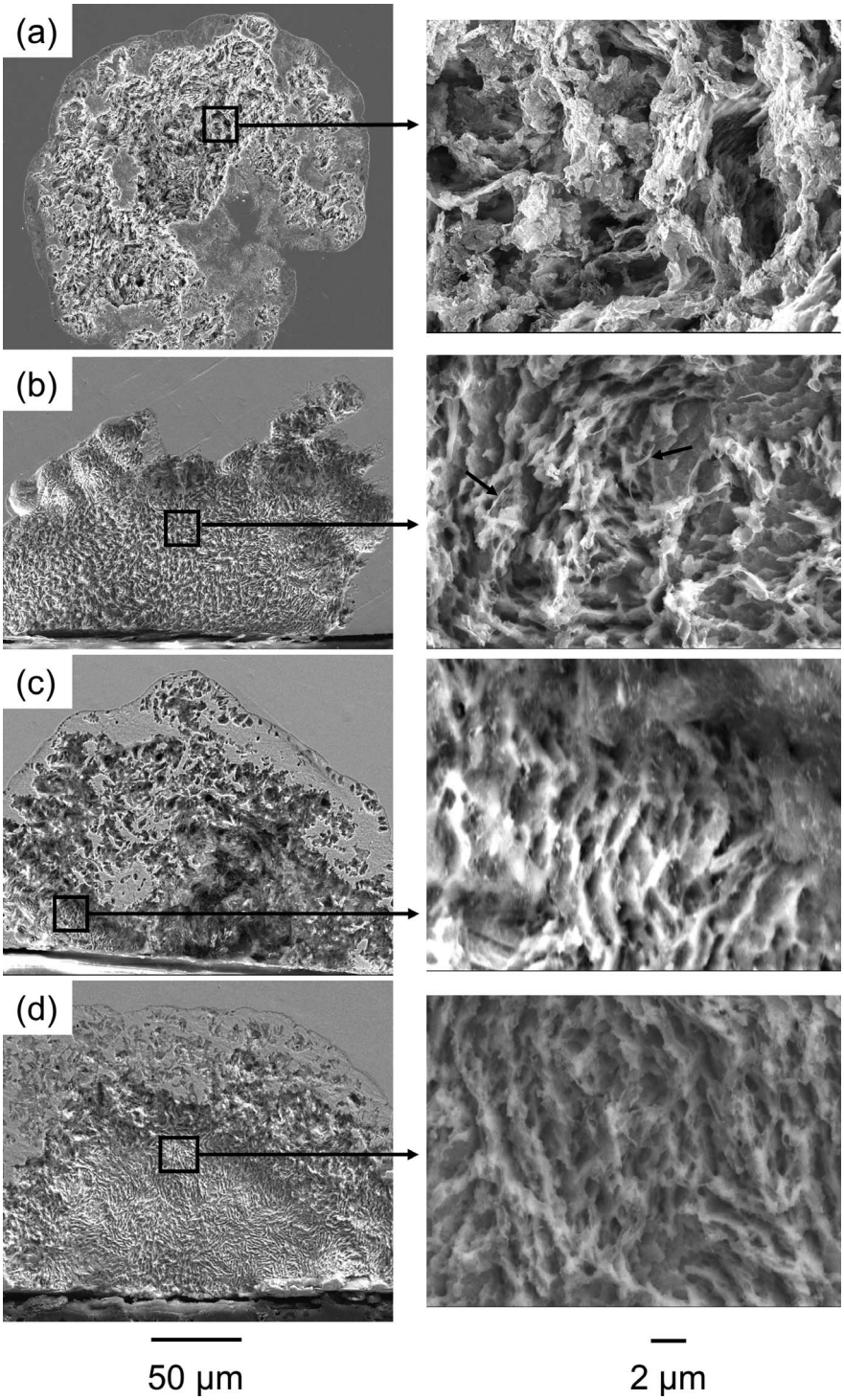

Figure 10. SEM images of pits on bulk Zr surfaces after anodic polarization (Figure 9) in (a) 0.9% NaCl; (b) 0.9% + 4% albumin; (c) 0.9% NaCl + 0.1% H_2O_2; (d) 0.9% NaCl + 0.1% H_2O_2 +4% albumin. Arrows indicated in part (b) show evidence of metal fragments inside the pit.

agreement No 659226 (Petre-Flaviu Gostin). Supplementary figures can be accessed via http://epapers.bham.ac.uk/3058/

ORCID

Yue Zhang https://orcid.org/0000-0003-2066-2821
Angus J. M. C. Cook https://orcid.org/0000-0002-9173-0863
Alison Davenport https://orcid.org/0000-0003-0853-515X

References

1. M. Niinomi, M. Nakai, and J. Hieda, *Acta Biomaterialia*, **8**, 3888 (2012).
2. X. L. Zhao, M. Niinomi, M. Nakai, T. Ishimoto, and T. Nakano, *Mater. Sci. Eng., C*, **31**, 1436 (2011).
3. P. Altuna, E. Lucas-Taulé, J. Gargallo-Albiol, O. Figueras-Álvarez, F. Hernández-Alfaro, and J. Nart, *Int. J. Oral Maxillofac. Surg.*, **45**, 842 (2016).
4. M. Chiapasco, P. Casentini, M. Zaniboni, E. Corsi, and T. Anello, *Clin. Oral Impl. Res.*, **23**, 1136 (2012).
5. S. Y. Yu and J. R. Scully, *CORROSION*, **53**, 965 (1997).
6. A. K. Mishra, J. A. Davidson, R. A. Poggie, P. Kovacs, and T. J. Fitzgerald, in *Medical Applications of Titanium and Its Alloys: The Material and Biological Issues*, S. Brown and J. Lemons Editors, p. 96, ASTM International, West Conshohocken, United States (1996).
7. I. Milosev, G. Zerjav, J. M. C. Moreno, and M. Popa, *Electrochim. Acta*, **99**, 176 (2013).

8. K. K. Wang, L. J. Gustavson, and J. H. Dumbleton, in *Medical Applications of Titanium and Its Alloys: The Material and Biological Issues*, S. Brown and J. Lemons Editors, p. 76, ASTM International, West Conshohocken, United States (1996).
9. R. Kondo, N. Nomura, Suyalatu, Y. Tsutsumi, H. Doi, and T. Hanawa, *Acta Biomater.*, **7**, 4278 (2011).
10. N. Nomura, Y. Tanaka, Suyalatu, R. Kondo, H. Doi, Y. Tsutsumi, and T. Hanawa, *Mater. Trans.*, **50**, 2466 (2009).
11. Suyalatu, R. Kondo, Y. Tsutsumi, H. Doi, N. Nomura, and T. Hanawa, *Acta Biomater.*, **7**, 4259 (2011).
12. M. L. Morrison, R. A. Buchanan, A. Peker, W. H. Peter, J. A. Horton, and P. K. Liaw, *Intermetallics*, **12**, 1177 (2004).
13. S. Hiromoto, A. P. Tsai, M. Sumita, and T. Hanawa, *Mater. Trans.*, **43**, 3112 (2002).
14. S. Hiromoto, K. Asami, A. -P. Tsai, M. Sumita, and T. Hanawa, *J. Electrochem. Soc.*, **149**, B117 (2002).
15. G. C. Palit and H. S. Gadiyar, *CORROSION*, **43**, 140 (1987).
16. M. Pourbaix, Atlas of Electrochemical Equilibria in Aqueous Solutions, *National Assiciation of Corrosion Engineers*, Houston, Texas, USA (1974).
17. N. T. C. Oliveira, S. R. Biaggio, R. C. Rocha-Filho, and N. Bocchi, *J. Biomed. Mater. Res., Part A*, **74A**, 397 (2005).
18. S. Virtanen, I. Milosev, E. Gomez-Barrena, R. Trebse, J. Salo, and Y. T. Konttinen, *Acta Biomater.*, **4**, 468 (2008).
19. M. A. Khan, R. L. Williams, and D. F. Williams, *Biomaterials*, **17**, 2117 (1996).
20. P. Hallam, F. Haddad, and J. Cobb, *J. Bone Jt. Surg., Br.*, **86B**, 27 (2004).
21. H. G. Willert, G. H. Buchhorn, D. Gobel, G. Koster, S. Schaffner, R. Schenk, and M. Semlitsch, *Clin. Orthop. Relat. Res.*, S160 (1996).
22. H. G. Willert and M. Semlitsch, *J. Biomed. Mater. Res.*, **11**, 157 (1977).
23. S. R. Golish and P. A. Anderson, *Spine J*, **12**, 693 (2012).
24. O. Addison, A. J. Davenport, R. J. Newport, S. Kalra, M. Monir, J. F. W. Mosselmans, D. Proops, and R. A. Martin, *J. R. Soc., Interface*, **9**, 3161 (2012).
25. F. Yu, O. Addison, and A. J. Davenport, *Acta Biomater*, **26**, 355 (2015).
26. B. Bozzini, P. Carlino, and C. Mele, *J. Mater. Sci.: Mater. Med.*, **22**, 193 (2011).
27. L. N. Wang, X. Q. Huang, A. Shinbine, and J. L. Luo, *J. Mater. Sci.: Mater. Med.*, **24**, 295 (2013).
28. D. Mareci, G. Bolat, R. Chelariu, D. Sutiman, and C. Munteanu, *Mater. Chem. Phys.*, **141**, 362 (2013).
29. L. C. Trinca, D. Mareci, N. Cimpoesu, M. Calin, and T. Stan, *Mater. Corros.*, **67**, 1088 (2016).
30. W. C. Xu, S. R. Street, M. Amri, J. F. W. Mosselmans, P. D. Quinn, T. Rayment, and A. J. Davenport, *J. Electrochem. Soc.*, **162**, C238 (2015).
31. S. R. Street, W. C. Xu, M. Amri, L. Y. Guo, S. J. M. Glanvill, P. D. Quinn, J. F. W. Mosselmans, J. Vila-Comamala, C. Rau, T. Rayment, and A. J. Davenport, *J. Electrochem. Soc.*, **162**, C457 (2015).
32. J. W. Tester and H. S. Isaacs, *J. Electrochem. Soc.*, **122**, 1438 (1975).
33. T. Rayment, A. J. Davenport, A. J. Dent, J. -P. Tinnes, R. J. K. Wiltshire, C. Martin, G. Clark, P. Quinn, and J. F. W. Mosselmans, *Electrochem. Commun.*, **10**, 855 (2008).
34. J. F. W. Mosselmans, P. D. Quinn, A. J. Dent, S. A. Cavill, S. D. Moreno, A. Peach, P. J. Leicester, S. J. Keylock, S. R. Gregory, K. D. Atkinson, and J. R. Rosell, *J. Synchrotron Radiat.*, **16**, 818 (2009).
35. M. Basham, J. Filik, M. T. Wharmby, P. C. Y. Chang, B. El Kassaby, M. Gerring, J. Aishima, K. Levik, B. C. A. Pulford, I. Sikharulidze, D. Sneddon, M. Webber, S. S. Dhesi, F. Maccherozzi, O. Svensson, S. Brockhauser, G. Náray, and A. W. Ashton, *J. Synchrotron Radiat.*, **22**, 853 (2015).
36. T. Roisnel and J. Rodriguez-Carvajal, *Mater. Sci. Forum*, **378**, 118 (2001).
37. B. Ravel and M. Newville, *J. Synchrotron Radiat.*, **12**, 537 (2005).
38. H. E. Swanson and R. K. Fuyat, *NatL. Bur. Stand. Circ. (US)*, **539**, 1 (1953).
39. B. Bondars, G. Heidemane, J. Grabis, K. Laschke, H. Boysen, J. Schneider, and F. Frey, *J. Mater. Sci.*, **30**, 1621 (1995).
40. A. Clearfield and P. A. Vaughan, *Acta Crystallogr*, **9**, 555 (1956).
41. J. Postlethwaite and M. Onofrei, *CORROSION*, **35**, 185 (1979).
42. M. Ghahari, D. Krouse, N. Laycock, T. Rayment, C. Padovani, M. Stampanoni, F. Marone, R. Mokso, and A. J. Davenport, *Corros. Sci.*, **100**, 23 (2015).
43. M. Monir, *XANES Study of Chemistry of Localized Corrosion in Artificial Pits of 316L Stainless Steel and Titanium* (*Ph.D. thesis*), University of Birmingham, Birmingham (2011).
44. C. B. Messner, T. S. Hofer, B. R. Randolf, and B. M. Rode, *Phys. Chem. Chem. Phys.*, **13**, 224 (2011).
45. A. J. Zielen and R. E. Connick, *J. Am. Chem. Soc.*, **78**, 5785 (1956).
46. C. Hagfeldt, V. Kessler, and I. Persson, *Dalton Trans*, 2142 (2004).
47. J. I. Langford and A. J. C. Wilson, *J. Appl. Crystallogr.*, **11**, 102 (1978).
48. M. Z. C. Hu, M. T. Harris, and C. H. Byers, *J. Colloid Interface Sci.*, **198**, 87 (1998).
49. R. Srinivasan, M. B. Harris, S. F. Simpson, R. J. De Angelis, and B. H. Davis, *J. Mater. Res.*, **3**, 787 (1988).
50. A. Clearfield, *J. Mater. Res.*, **5**, 161 (1990).
51. R. C. Garvie and M. V. Swain, *J. Mater. Sci.*, **20**, 1193 (1985).
52. M. E. Nagassa, A. E. Daw, W. G. Rowe, A. Carley, D. W. Thomas, and R. Moseley, *Clin. Oral Implants Res.*, **19**, 1317 (2008).
53. Y. Zhang, *Corrosion of Titanium, Zirconium and Their Alloys* (*Ph.D. thesis*), University of Birmingham, Birmingham (2017).